



THE UNIVERSITY *of* EDINBURGH

Edinburgh Research Explorer

## Design of a Hall effect sensor controlled brittle star inspired composite robotic limb

### Citation for published version:

Mack, J & Alam, P 2022, 'Design of a Hall effect sensor controlled brittle star inspired composite robotic limb', *Engineering Research Express*, vol. 4, no. 3, 036001. <https://doi.org/10.1088/2631-8695/ac90ac>

### Digital Object Identifier (DOI):

[10.1088/2631-8695/ac90ac](https://doi.org/10.1088/2631-8695/ac90ac)

### Link:

[Link to publication record in Edinburgh Research Explorer](#)

### Document Version:

Publisher's PDF, also known as Version of record

### Published In:

Engineering Research Express

### General rights

Copyright for the publications made accessible via the Edinburgh Research Explorer is retained by the author(s) and / or other copyright owners and it is a condition of accessing these publications that users recognise and abide by the legal requirements associated with these rights.

### Take down policy

The University of Edinburgh has made every reasonable effort to ensure that Edinburgh Research Explorer content complies with UK legislation. If you believe that the public display of this file breaches copyright please contact [openaccess@ed.ac.uk](mailto:openaccess@ed.ac.uk) providing details, and we will remove access to the work immediately and investigate your claim.



NOTE • OPEN ACCESS

## Design of a Hall effect sensor controlled brittle star inspired composite robotic limb

To cite this article: Jonah Mack and Parvez Alam 2022 *Eng. Res. Express* 4 036001

View the [article online](#) for updates and enhancements.

You may also like

- [Progress in Graphene Synthesis and its Application: History, Challenge and the Future Outlook for Research and Industry](#)  
Kartika A. Madurani, Suprpto Suprpto, Nur Izzati Machrita et al.
- [Polyfluorinated organic compounds of boron](#)  
Nicolay Yu Adonin and Vadim V Bardin
- [Applications of Carbon Nanotubes Grown by Chemical Vapor Deposition](#)  
John Robertson, Guofang Zhong, C. Santiago Esconjauregui et al.



## NOTE

## Design of a Hall effect sensor controlled brittle star inspired composite robotic limb

## OPEN ACCESS

RECEIVED  
15 July 2022REVISED  
17 August 2022ACCEPTED FOR PUBLICATION  
8 September 2022PUBLISHED  
16 September 2022

Jonah Mack and Parvez Alam\*

School of Engineering, The University of Edinburgh, Edinburgh, EH8 9YL, United Kingdom

\* Author to whom any correspondence should be addressed.

E-mail: [j.mack-1@sms.ed.ac.uk](mailto:j.mack-1@sms.ed.ac.uk) and [parvez.alam@ed.ac.uk](mailto:parvez.alam@ed.ac.uk)

Keywords: motion control, bioinspired robot, robotics, ambulate robot, pentapod

Original content from this work may be used under the terms of the [Creative Commons Attribution 4.0 licence](https://creativecommons.org/licenses/by/4.0/).

Any further distribution of this work must maintain attribution to the author(s) and the title of the work, journal citation and DOI.



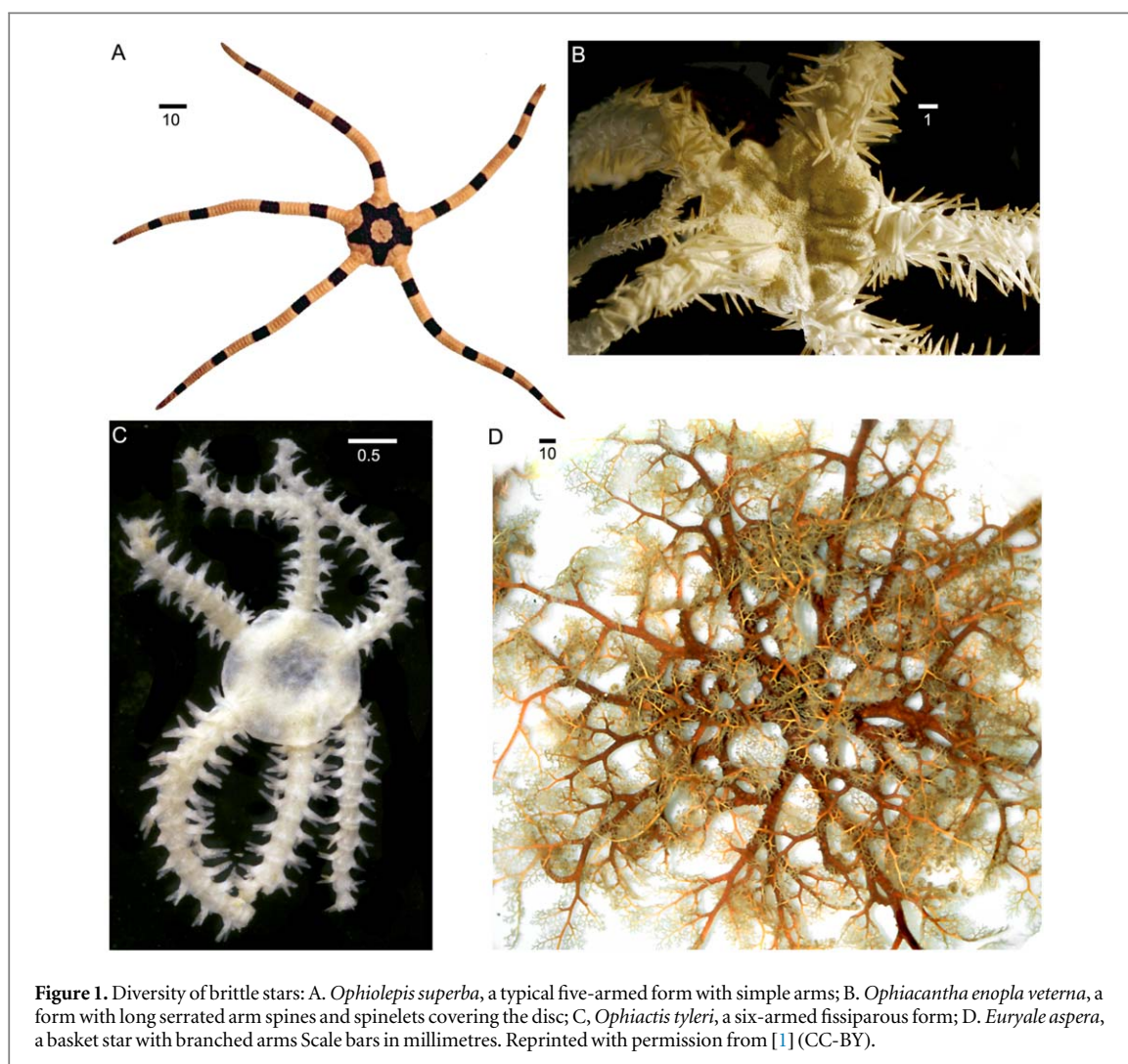
## Abstract

This paper elucidates a method of actuation and feedback for hard-soft composite continuum pentapod appendages to enable both kinematic accuracy and gait. A feedback mechanism based on Hall effect sensors is integrated within a hard exterior/soft interior composite robotic limb, which is unaffected by actuator slippage, and provides accurate (sub  $2^\circ$ ) end point measurements. The proposed method for actuation uses two actuators to control a full semi-spherical range of motion, an improvement to the use of three actuators more commonly reported in the literature. When applied to enable the gait of a complete brittle star inspired pentapod, we find that our design reaches a momentum of  $0.52 \text{ kg} \cdot \text{m s}^{-1}$ , surpassing the momentum of previously reported untethered starfish inspired pentapods by 3.7 times.

## 1. Introduction

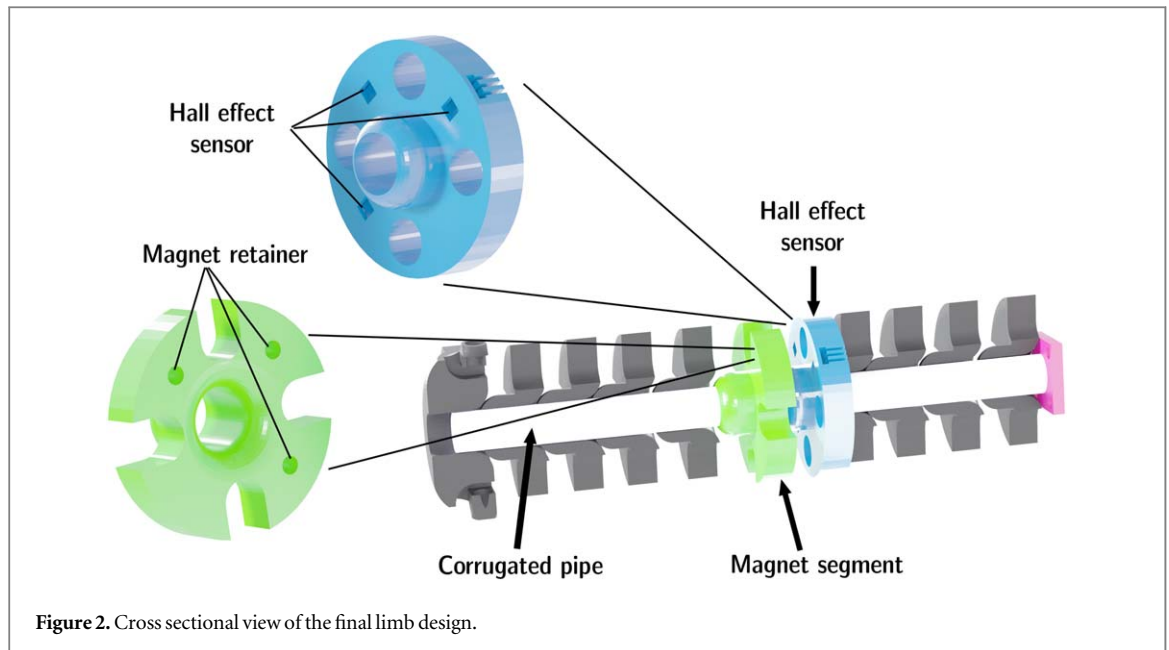
Brittle stars are diverse echinoderms, figure 1, in the class of Ophiuroidea, closely related to starfish [1]. They have five flexible arms with lengths varying from 0.3–60 cm [2]. While brittle stars are pentapedal animals, they have the capacity for movement using lower numbers of limbs (down to bipedal motion), and have sufficient versatility to be able to navigate a range of different terrains. They also have the capacity to climb, crawl and swim and as such, exhibit superior levels of natural actuation when compared against other echinoderms. Mechanically, brittle star limbs are different to those of other high degrees of freedom (DoF) animal limbs (e.g. legs and tentacles) such as in octopus, squid and cuttlefish. While flexibility in these animals is simplified by material softness, brittle stars have much tougher exteriors and their limbs are thus segmented and joined.

The challenge in developing brittle star inspired pentapod (5-legged) robots is, therefore, in coupling the mechanical design of a functional tough exterior/soft interior composite leg with viable high DoF motion control. The benefits of such a configuration is to allow the coupling of desirable aspects of soft robotics with those of hard exterior robots. The combination of these features means that the robot can morph its shape with higher degrees of deflection than that of a rigid bodied robot, and has additional benefits in dynamic mechanical or impact energy dissipation, due to there being a flexible continuum. The coupled rigid exterior enables the robot to be used in environments and under conditions where a soft flexible robot body may suffer from external damage such as punctures from contact with sharp objects. The pentapod is a unique area of robotics that has received considerably less attention than other n-legged robots such as bi-, tri-, quadru- and hexapods [3–6]. Actuation control in pentapodal robotics is not always trivial. There are a number of factors to consider including the large numbers of possible forms of gait, methods for actuation, the suitability of the mechanical design of the limb in terms of both limb-loading and kinematics, the actuation mechanism for an individual limb incorporating high DoF, and sense-response mechanisms devoted to motion control. Jin and Dong [3] considered Shape Memory Alloy (SMA) actuation systems for starfish inspired pentapods with limited DoF. Their pentapodal robots had modular legs that were mechanically designed to actuate in only one axis. This is not as versatile as the actual starfish and the design therefore has obvious limitations in terms of bioinspired gait.



Some mechanical designs make use of a decentralised control system like that of the brittle star [5, 6] where the arms make use of two to three servos per arm to control the vertical and horizontal motion of each leg. In [5] and [6] each leg uses an individual Proportional Derivative (PD) controller and a pre-determined motion path for the gait. As evidenced by [6], stability analyses for 22 gait combinations, a  $3 \times 2$  gait sequence is optimal for pentapodal speed. Research into climbing gaits [7, 8] has been conducted to optimise pentapodal climbing, but it cannot be assumed that this transfers naturally into walking gaits. Performance metrics for various n-legged gaits demonstrate that soft-body starfish inspired robots [4] are unable to move as effectively as other n-legged robots [5]. However, they are less complex in terms of gait sequence and because they are pentapodal, they have a large variety of gait sequences that may be of benefit for other-than flat terrain walking situations.

Starfish-inspired robots are either soft-body SMA actuated robots, or, are fully rigid hard body robots. The closest robot to bridging the gap between these, offering higher levels of dynamic motion to that of current soft-body robots is PATRICK [4]. This robot has an untethered design, utilising two SMA actuation wires in a highly flexible silicon limb to generate more complex motion paths than other soft-body robots. PATRICK is one of the first untethered brittle star inspired underwater robots that in real-time varies its locomotion. Almost all of the compute for PATRICK is executed remotely on a laptop, so the robot is less viable for real world applications without a remote laptop connection. Displacement over time metrics are also given for PATRICK, and it can be noted from these metrics that the robot performs well for its relative scale and soft-body make up. It appears that [4] is the only work to propose a closed-loop trajectory planning method of motion primitives in a 5-legged robot. One of the key areas of improvement mentioned is to move the compute on-board the starfish so that it can be used in a non-lab environment. Along with this, it is important to note that PATRICK needs to operate under water due to the cooling requirements of the SMA wires, meaning it would not perform to the same level out of water if the temperatures are sufficiently high to prevent the effective utility of SMA wires. A key short-coming of the mechanical design of PATRICK is that of inter-limb variance. This was noted to be due to the limb



force output and displacement being sensitive to differences in manufacturing. In addition, the SMA wires coupled with the silicon limbs introduce a level of significant non-linearity to the system.

Effective position control is a function of system mechanics, material properties, the method of actuation and the accuracy and speed of sense-response mechanisms during actuation. The robotic limb reported in this communication considers all four functions. Our aim is to design a brittle star inspired mechanical limb with high degrees of motive freedom enabled by minimised numbers of actuators. The robotic limb will, like the brittle star, combine a hard exoskeleton with a soft and flexible internal segment to enable a shared material, composite response to actuation. Finally, a Hall effect sensor system will be designed as an integral part of the limb itself, as we hypothesise that this will minimise position control errors that may ordinarily arise from mechanical losses during actuation and inaccurate controller feedback. Our hypothesis is based on that Hall effect sensors have already been shown to be effective in soft appendage robotic control. Proprioceptive sensing in soft limb robots for example [9], has been improved through modifications of the Hall effect curvature sensor alongside modifications to the actuation chamber cross section, which if soft, requires advanced flexible sensing mechanisms such as has been reported in [10]. Soft actuating limbs using groups of three-linear sensors are known to enable a high level of accuracy in soft robotic limb movement in flexure [11, 12] and as such, are considered in this work to also have potential for the soft-hard composite appendages intended in this work.

## 2. Materials, Methods and Design Philosophy

### 2.1. Mechanical Design

Mechanical design was driven by two main parameters, a soft-body level of bending and curvature with a harder exterior (like the actual brittle star), and reliable motion to improve on designs described in existing literature. Due to mechanical limitations in existing brittle star inspired designs, inspiration was sought elsewhere, including both the actual brittle star and other areas of robotics. 3D brittle star models [2] have enabled researchers to gain a deeper understanding of the mechanical structuring of the limb. The structure is essentially made up of discrete segments that interconnect via a ball and socket-like joint. Connective tissues and ligaments maintain the position and interlocking of the limbs. The use of repeat segments in the brittle star limb allows it to exhibit high degrees of curvature and mobility. The robotic structure mimicked herein and rendered in CAD, figure 2, uses a flexible corrugated polypropylene pipe allowing for high degrees of deflection in Euclidean space [13, 14]. FDM printed PLA exoskeletal segments are slipped over the polypropylene pipe and interlocked to mimic the exterior interlocked brittle star structure inferred from [2]. Segment to segment interlocking aids mobility in the exterior skeleton through its simple design, which is a tapered end interlocking protuberance from one segment that is inserted into the opening of an adjacent segment. Once inserted, the interlocking mechanism has a high degree of rotational freedom, similar to that of a ball and socket joint. The Hall effect sensors shown in figure 2 are embedded into external segments, and these are used to monitor movement. Further details on the sensor feedback is provided in section 2.3.

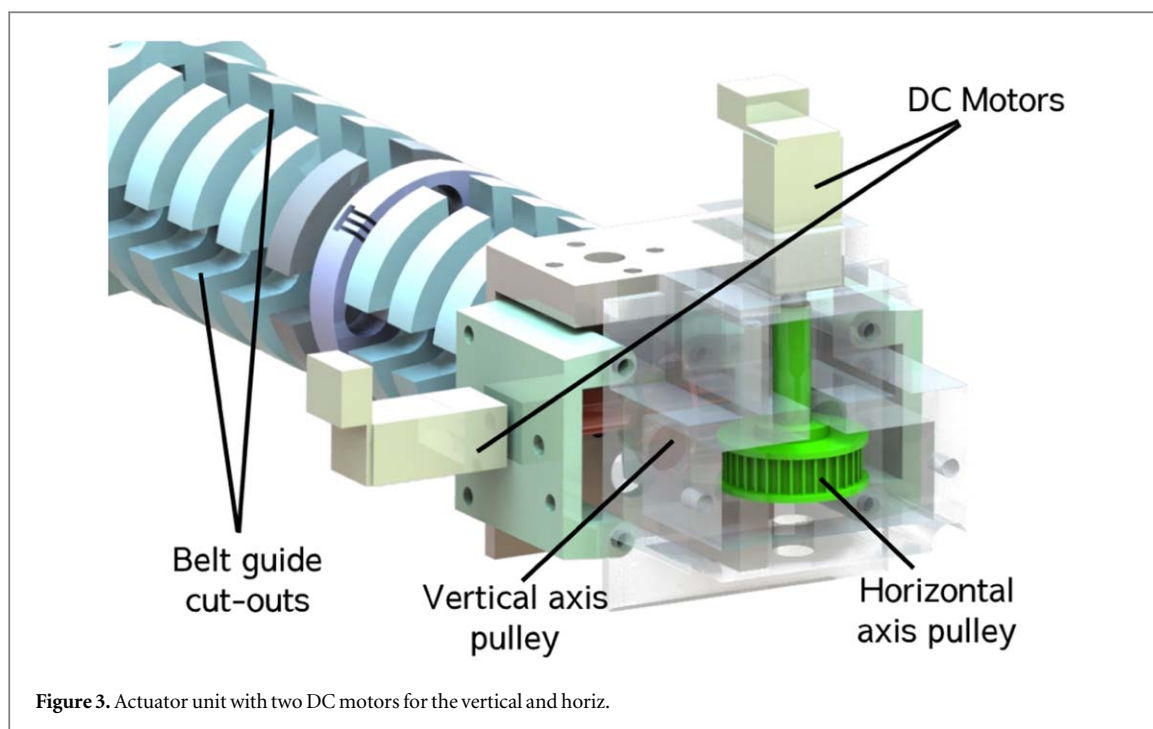


Figure 3. Actuator unit with two DC motors for the vertical and horiz.

## 2.2. Actuator Design

Inspiration was drawn from continuum style robotic manipulators [15–17]. A continuum robot relies on a bendable and often compliant central core, which in the case of our design is a polypropylene corrugated pipe described in section 2.1. The single rod core design was pioneered by [18] and has the benefit of enabling non-complex deformation under loading.

Actuation in our design, figure 3, relies only on two actuators to achieve a full range of motion, an improvement to the commonly seen set of three. To keep the arm itself light and small we selected an extrinsically actuated continuum [19], figure 4. The use of a GT2 timing belt driven design as opposed to a metal or polymer pulley [20] ensures there is a reliable connection between the leg and actuator with minimal slip or mechanical losses. The driven belt allows for a single pulley wheel to pull the continuum arm in the two primary directions along a single plane, figure 5. Doing this with two orthogonally oriented pulley wheels enables a full envelope of actuation with only two actuators. The use of two actuators on a toothed driven belt analogous to a tendon is a novel concept in continuum robotics, as many existing designs rely on a polymer pulley, and often, on more than two actuators to achieve the same DoF as we have in our design [17, 21, 22].

## 2.3. Hall Effect Sensor Feedback

A key component in dynamic robot design is the accurate feedback of limb positions to the controller for improved control of the limb in its inertial state. A Hall effect sensor position feedback solution, similar to that of [23], for the end point of the leg was implemented to provide the robot with useful limb-endpoint information. The application of this configuration in a hard-exterior limb is a novel application of the Hall effect array. Due to the nature of soft robotics, determining the orientation of a soft-bodied limb is difficult due to the infinite possible passive joint positions [24]. Similar work done on soft robot curvature presented by [25] and [26], uses a single Hall effect sensor to measure out of plane bending. Here, we use a  $3 \times 3$  array of Hall effect sensors to feedback position. Similar systems have been used to monitor loading and unloading of spinal columns [27] and in orientation resolution of a spherical actuator [28]. Since Hall effect sensors and sensor arrays have been shown to have high accuracy for distance/orientation measurement [25, 28, 29], the use of Hall effect sensors in the continuum limbs of our robotic limb offers a small form factor but with the potential for high accuracy.

### 2.3.1. Orientation Resolution

The GT2 timing belt in our design connects the actuator to the limb and as such, slip is a possibility in any situation that may drive a force overload. A magnetic encoder such as used in [22], attached directly to the drive shaft of the actuator would not be able to provide sufficient information on the position of the limb in our design and furthermore require a calibration loop, and thus unable to offer absolute orientation of the limb in a continuum limb. Three points can be used to define a plane and as such, three Hall effect sensors is the minimum possible number that can be used to derive information on the planar orientation of the limb segment

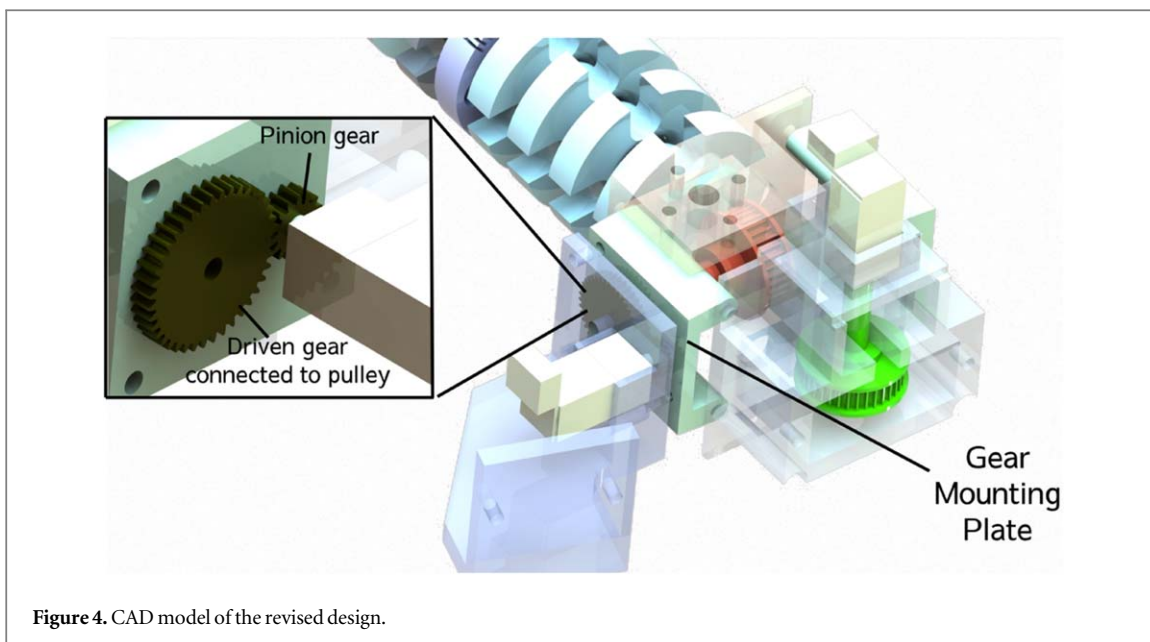


Figure 4. CAD model of the revised design.

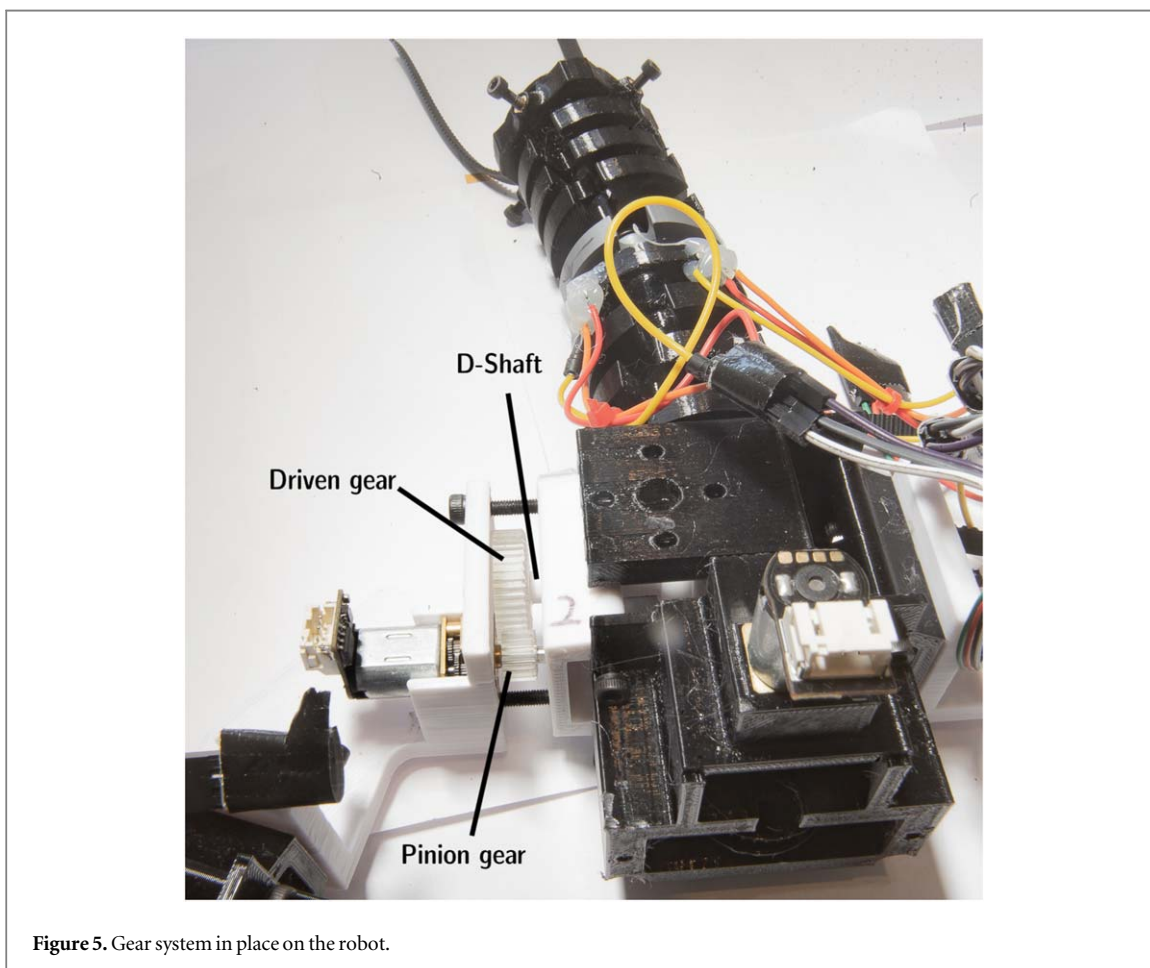


Figure 5. Gear system in place on the robot.

containing the sensors. This feedback arrangement relies on the assumption that the planar orientation of the middle section can be extrapolated to provide information on the end point of the limb. Our control system differs from that of previous work [4, 30] in that they used single value decomposition with a proportional integral controller to provide orientation control to an SMA actuated soft limb.

The only criterion to determine a plane with three points is that the three points are not co-linear. From figure 6 it is immediately obvious that the three points are not co-linear. These points are given coordinates

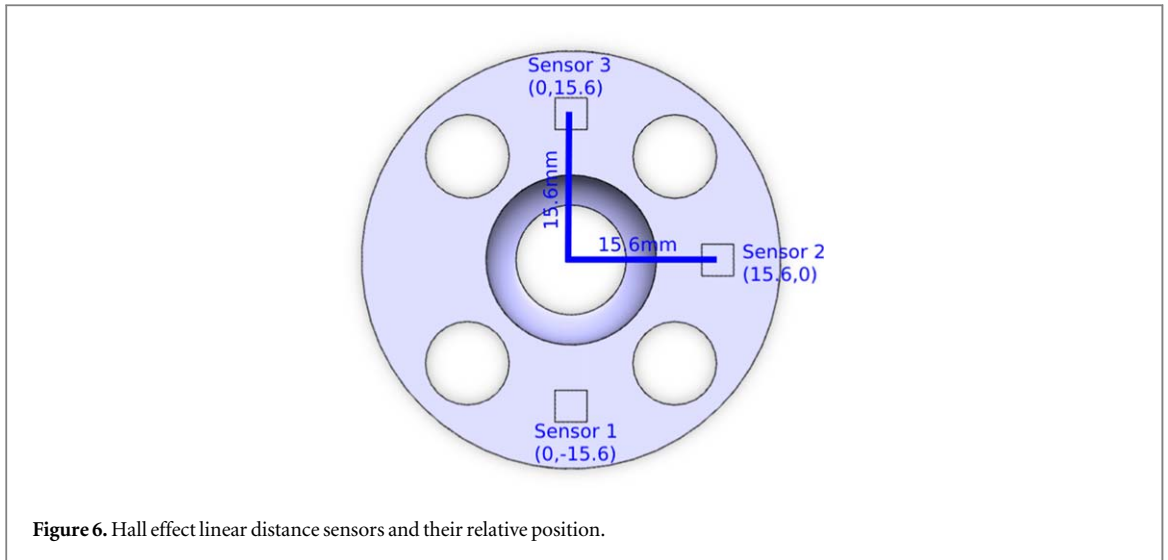


Figure 6. Hall effect linear distance sensors and their relative position.

relative to the center of the segment. The adjacent segment in the leg design has three circular holes that hold permanent magnets at the exact same coordinates as the adjacent sensors. As the orientation of this adjacent segment moves, the relative distance of the magnets to the sensors changes, thus allowing the orientation to be determined. This relative distance is what makes up the  $z$  component of the coordinates to define the plane in 3-dimensions. The  $x, y$  position of the sensors do not align with the principle axis of motion for the pulley system. Therefore, a rotation matrix had to be applied to the readings so that the resolved vectors were in alignment with the new reference frame. The rotation matrix is used with  $\theta = \frac{\pi}{4}$ . Where  $x_{n,new}$  and  $y_{n,new}$  represent the adjusted  $x, y$  coordinates of the sensor locations.

$$\begin{bmatrix} x_{n,new} \\ y_{n,new} \end{bmatrix} = \begin{bmatrix} \cos \theta & -\sin \theta \\ \sin \theta & \cos \theta \end{bmatrix} \begin{bmatrix} x_n \\ y_n \end{bmatrix} \quad (1)$$

Two vectors are created using the real-time measurements from the Hall effect sensor, and are given as  $z_n$  where  $n$  corresponds to the sensor number the respective measurement is taken from according to figure 6.

$$V_1 = (x_2 - x_1, y_2 - y_1, z_2 - z_1) \quad (2)$$

$$V_2 = (x_2 - x_3, y_2 - y_3, z_2 - z_3) \quad (3)$$

With these two vectors we can find the normal ( $N$ ) via the cross product, where the constituent components of  $N = [N_x \ N_y \ N_z]$ .

$$N = V_1 \times V_2 \quad (4)$$

The angles between the normal vector and its two constituent vectors can be found, these angles, as demonstrated in figure 7, are  $\psi$  and  $\theta$ . Where  $\psi$  denotes the axis from sensor 2 to sensor 1, and  $\theta$  the axis from sensor 2 to sensor 3.

$$\psi = \arccos\left(\frac{N_x}{|N|}\right) \quad (5)$$

$$\theta = \arccos\left(\frac{N_y}{|N|}\right) \quad (6)$$

The simplified deflection model shown in figure 8 shows how the orientation from the sensor readings can be used to find the end point location in one dimension.

### 2.3.2. System Dynamics

With the method of feedback established, the actuator dynamics was introduced to enable limb control. A desired end point will be provided in spherical coordinates, as denoted by  $\theta_p$  and  $\psi_p$ . The error in the current state of the arm and the desired state can then be given as in equation (7), with the same equation being used for  $\psi$ .

$$error_{\theta} = \theta_p - \theta \quad (7)$$

A relationship between the end limb position and actuator was established via the simplified dynamics of the system. The motor speed was controlled via a pulse width modulation (PWM) signal. However, it is assumed



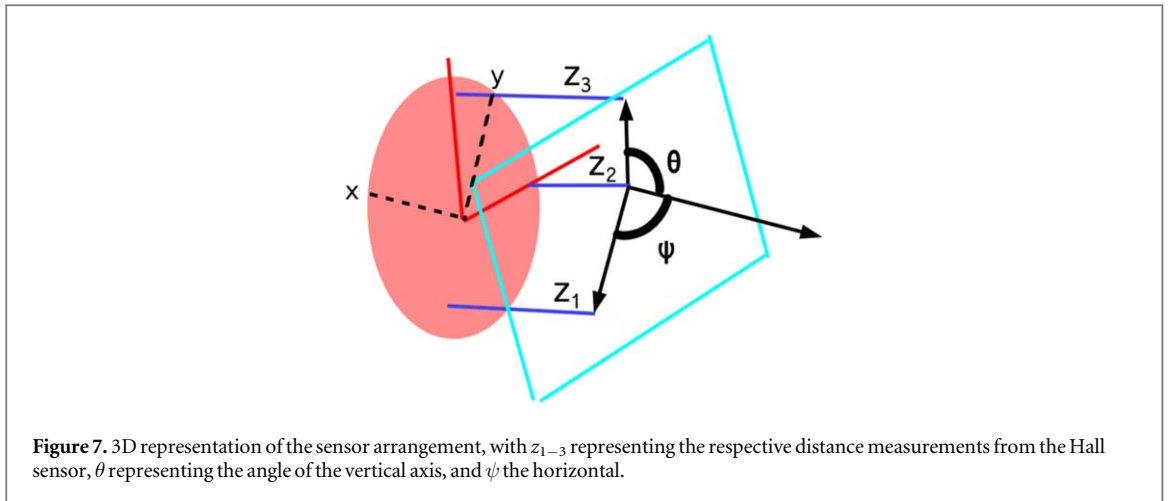


Figure 7. 3D representation of the sensor arrangement, with  $z_{1-3}$  representing the respective distance measurements from the Hall sensor,  $\theta$  representing the angle of the vertical axis, and  $\psi$  the horizontal.

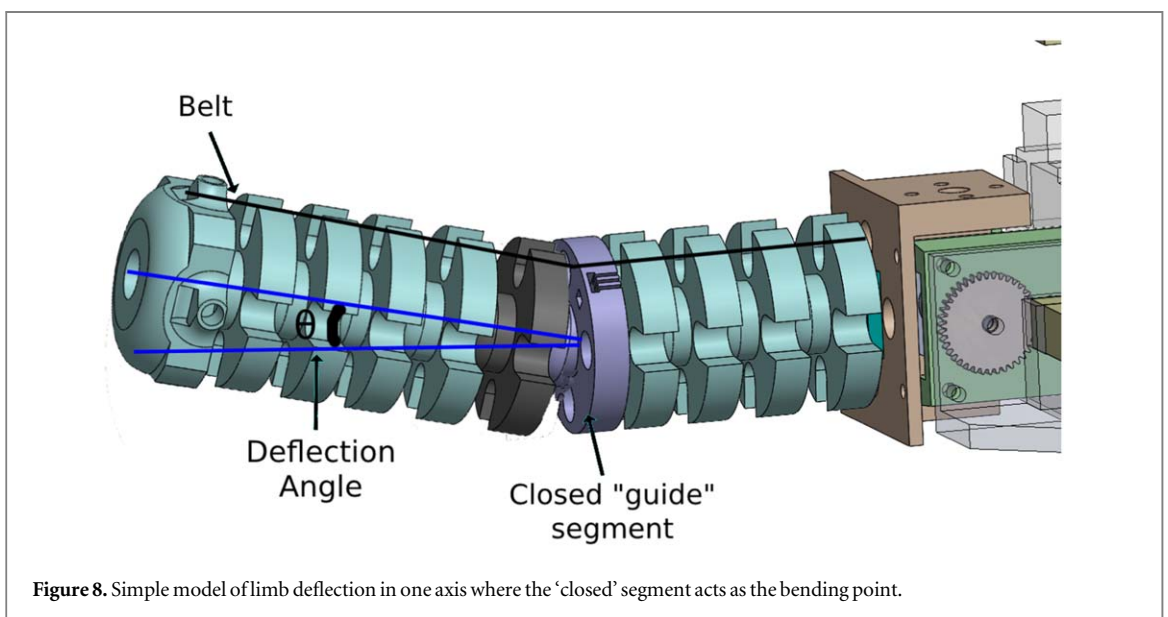


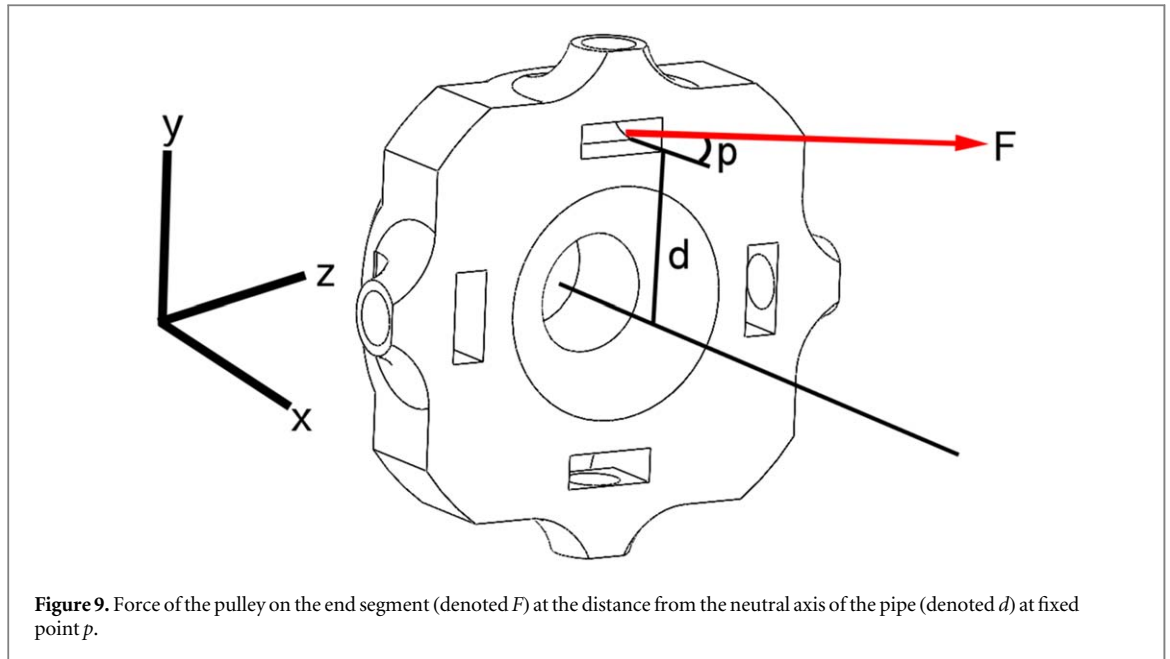
Figure 8. Simple model of limb deflection in one axis where the 'closed' segment acts as the bending point.

that the PWM signal is analogous to the force applied from the motor. The signal was split from 0 to 180, with 90 being stationary, 0 being maximum speed counterclockwise and 180 being maximum speed clockwise. A linear relationship was developed using the analogous force and torque specifications of the motor and gearbox as  $F = \frac{28}{90}(x - 90)$ . The motor can produce a maximum 2.9 kg · cm (0.28 N · m) of torque, given a pulley with radius 1 cm the motor produces a pulling force on the beam of 28N. Noting that due to the inclusion of the gear reduction for the vertical axis the force equation is multiplied by 2.66,  $F = 2.66(\frac{28}{90}(x - 90))$ , where  $F$  is the resulting force and  $x$  is the PWM signal.

Similar to the work done in [30], the deflection of the arm can be estimated using Euler-Bernoulli beam mechanics, where the arm is represented as a cantilevered beam. The true system dynamics are complex, as the arm moves the vector of the pulling force  $F$  changes relative to the arm. To simplify this, the motion is simplified to one dimension; the force applied is broken down to a vertical component ( $F_y$ ) acting as a point load at the tip, and the horizontal component ( $F_x$ ) acting as an end moment, as demonstrated in figure 9. This is then linearised around the point of investigation (denoted  $p$ ), equation (8).

$$\theta = \frac{F \cos(p)dL}{EI} + \frac{F \sin(p)L^2}{2EI} \tag{8}$$

This is identical to the equation used for  $\psi$ . Where  $F$  is the force applied  $d$  distance away from the center of the beam.  $L$  represents the length of the beam,  $E$  is the Young's Modulus of the polypropylene pipe (1325 MPa [31]) and  $I$  the second area moment of inertia. Combining the equations for force this expands to  $\theta = \frac{2.66(\frac{28}{90}(u_1 - 90))\cos(p)dL}{EI} + \frac{2.66(\frac{28}{90}(u_2 - 90))\sin(p)L^2}{2EI}$  with  $u_1$  representing the vertical motor PWM signal and  $u_2$  representing the horizontal motor signal. The simple model lends itself to ease of compute, an important aspect



considering there is 5 legs that will each run through this process. The plant for the system  $G(s)$  can now be established as in equation (9).

$$G(s) = \left[ \begin{array}{c} \frac{5.32(\frac{29}{90})\cos(p)dL + 2.66(\frac{29}{90})\sin(p)L^2}{EI} \\ \frac{2(\frac{29}{90})\cos(p)dL + (\frac{29}{90})\sin(p)}{EI} \end{array} \right] \quad (9)$$

The offset of 90 is introduced to the control signal outside of the plant. A PI controller is introduced as  $H(s)$ , equation (10).

$$H(s) = \left[ \begin{array}{c} 0.375k_p + 0.375k_i \frac{1}{s} \\ k_p + k_i \frac{1}{s} \end{array} \right] \quad (10)$$

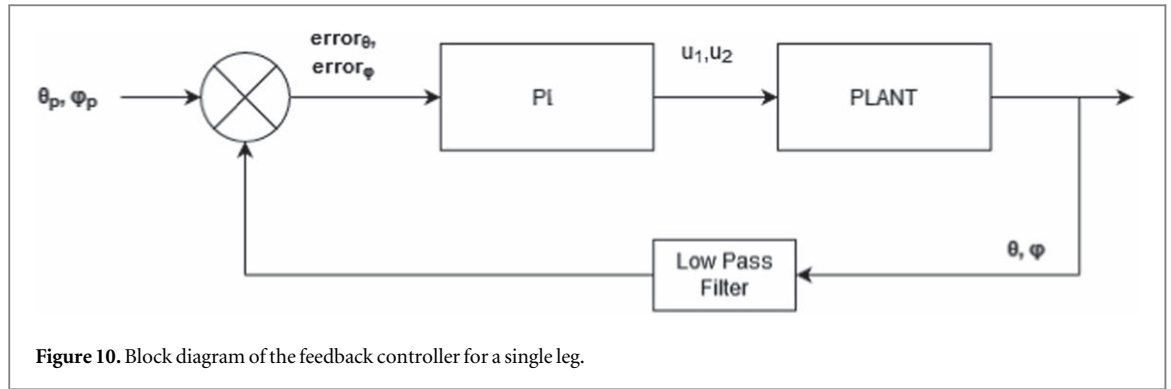
Where  $k_p$  is the proportional gain and  $k_i$  the integral gain. Row 1 has the gains multiplied by a factor of 0.375 as the force output of the vertical motor is over twice that of the horizontal, allowing the system to be tuned once. The dynamics of the appendage is not only a function of the mechanical parameters but is also affected by the control parameters. Here, our focus is on evidencing an accurate mechanical response based on a novel Hall effect sensor system and we therefore maintain consistent control parameters to more effectively detail these mechanical responses.

### 2.3.3. Controller Implementation

The reading from the Hall effect sensor is fed into the micro-controller as a voltage. This is interpreted as an analog signal with a value of 0–1025 (with 0 being 0 volts and 1025 being 5 volts). As such, an initial calibration of the sensor is needed, after which the values can be stored. In real-time use, the analog signal from the Hall effect sensor is relatively noisy. A first-order low-pass filter was thus implemented to smooth out the noise, hence removing actuation errors arising as a function of noise, equation (11), where  $\alpha$  represents the filter constant. With  $\hat{z}$  representing the filtered reading for the sensor given the current reading at time  $t$  (denoted  $z_t$ ). The full control block diagram can then be designed, figure 10, thus closing the loop for end-point control of the continuum limb. This process is repeated across all 5 limbs of the starfish robot, such that any end point position could be given to any limb and the desired position achieved.

$$\hat{z} = \alpha \cdot z_{t-1} + (1 - \alpha) \cdot z_t \quad (11)$$

The block diagram above was modelled in MATLAB's simulink utility and the PI controller tuned. Controller response to a step response input, such as noise from the analog Hall effect sensors, was verified. Non-linearities in the model were introduced to ensure the sim-to-reality differences are minor.



## 2.4. Numerical Simulation

A numerical model was developed to provide additional validation on the accuracy of the analytical model. As previously established, the singular leg can be simplified into a planar model. The left side of the model has a closed off section that represents the interface between the actuator housing and the corrugated pipe continuum. This is the fixed point condition of the limb, as shown in figure 13. At the height of the pulley a point load was applied in the  $-x$  and  $+y$  direction to approximate the components of the force vector from the pulley will load the beam. The model was discretised using Lagrange quadratic elements and a linear elastic analysis solved using a direct UMFPAK. A final mesh consisting of 268 480 elements was deemed appropriate for the simulations following a mesh convergence analysis. Polypropylene was modelled with a Young's modulus of 3.275GPa, while the PLA was modelled with a Young's modulus of 2.9GPa. A point load was applied based on equation (8) and the base-end of the limb was assigned a Dirichlet condition (0 DoF). A force of 21N was thus applied to achieve a deflection of  $30^\circ$ . The individual forces in the  $x$  and  $y$  directions from this point give a resultant force of 21N  $30^\circ$  from the loading point. The plane stress model was generated using the underlying constitutive plane stress equation, equation (12), where  $\sigma_{11}$  and  $\sigma_{22}$  are normal stresses in orthogonal directions,  $\sigma_{12}$  is the shear stress relative to these directions,  $\nu$  is the Poisson's ratio,  $\varepsilon_{11}$  and  $\varepsilon_{22}$  are normal strains in orthogonal directions, and  $\varepsilon_{12}$  is the shear stress relative to these directions.

$$\begin{bmatrix} \sigma_{11} \\ \sigma_{22} \\ \sigma_{12} \end{bmatrix} = \frac{E}{1 - \nu^2} \begin{bmatrix} 1 & \nu & 0 \\ \nu & 1 & 0 \\ 0 & 0 & \frac{1 - \nu}{2} \end{bmatrix} \begin{bmatrix} \varepsilon_{11} \\ \varepsilon_{22} \\ 2\varepsilon_{12} \end{bmatrix} \quad (12)$$

## 2.5. Pentapod robot locomotion

A whole body controller (WBC) and gait scheduler was developed to enable advanced robot locomotion. End-point limb control was used in accordance with a holistic controller and motion planner for dynamic motion of the robot. A BMI088 inertial measurement unit (IMU) was attached to the central body to measure the inertial state of the robot, the body axis for which is shown in figure 11. This measures the angular rate around 3 axis and the linear acceleration in those 3 axis, equations (13) and (14), where  $v_{gyro}$  has 3 measurements, the angular velocity, around  $x, y, z$  axis, and the same with  $v_{accel}$  where the 3 measurements are the linear accelerations in each direction. Utilising concepts from [32], the absolute orientation of the IMU can be determined by the use of quaternion vectors and a basic gradient descent loop. As described in [32], A quaternion is a four-spatial-dimension complex number that can be mapped into three dimensions to track orientation, equation (15). The advantage of quaternion orientation representation is the removal of gimbal lock, which enables a higher range of orientation conditions  $>90^\circ$ , if the need arises.

$$v_{gyro} = \begin{bmatrix} 0 & \omega_x & \omega_y & \omega_z \end{bmatrix} \quad (13)$$

$$v_{accel} = \begin{bmatrix} 0 & a_x & a_y & a_z \end{bmatrix} \quad (14)$$

$$q = [q_1 \quad q_2 \quad q_3 \quad q_4] \quad (15)$$

Quaternion multiplication is non-commutative, as a result of the Hamilton rule. The full cross product is given by [32], and it is of note that the cross product is non-commutative for quaternion multiplication. Given a gyroscopic reading vector from the IMU the orientation can be represented with a quaternion, equation (16), which creates a derivative quaternion ( $\dot{q}$ ) using the gyroscopic input from the IMU. With this, the quaternion can be numerically integrated in code to provide a quaternion representing the orientation of the robot ( $q_{est,t}$ ), equation (17), given the current quaternion  $q_t$ , the previous quaternion estimate output  $q_{t-1}$ , and the time between the last calculation and the current one  $\Delta t$ .

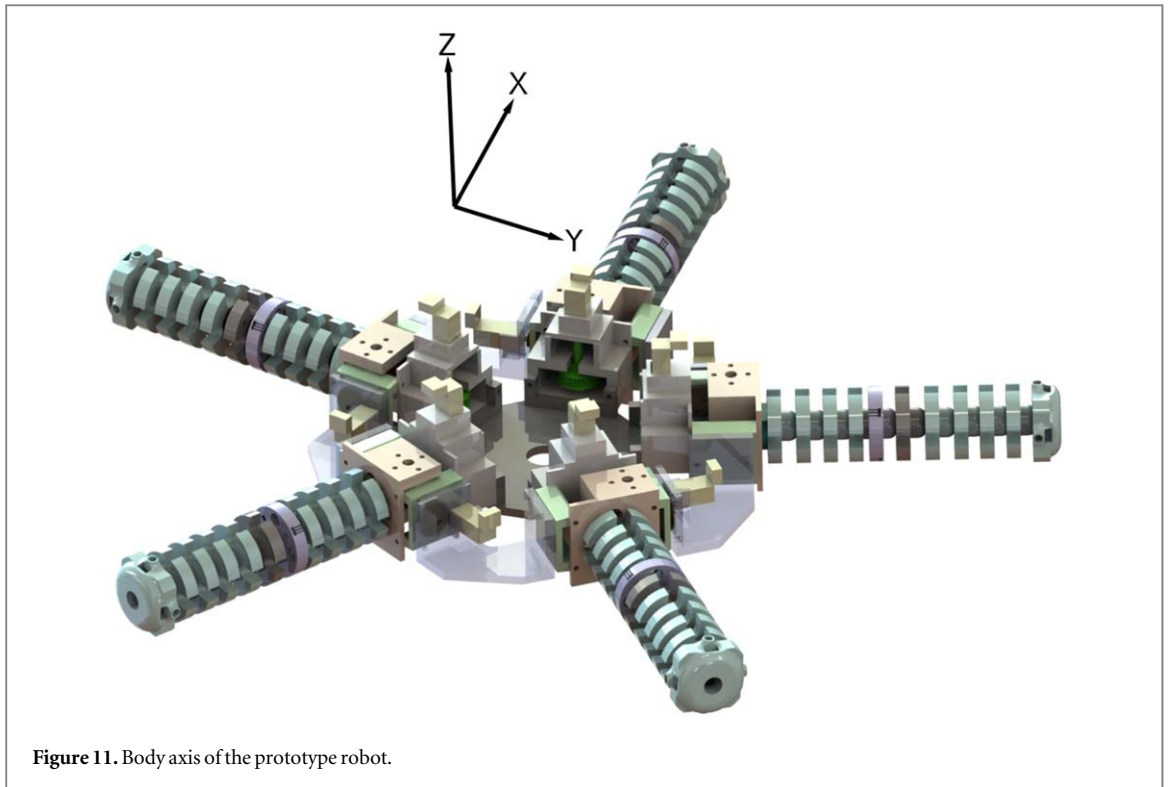


Figure 11. Body axis of the prototype robot.

$$\dot{q} = 0.5 \cdot q \times v_{gyro} \quad (16)$$

$$q_{est,t} = 0.5 \cdot q_{t-1} + q_t \cdot \Delta t \quad (17)$$

The introduction of the accelerometer is described in length by [32], for context, equation (18) shows how the accelerometer is introduced alongside the estimated quaternion from equation (17).

$$f_g(q_{est}, v_{accel}) = \begin{bmatrix} 2(q_2q_4 - q_1q_3) - a_x \\ 2(q_1q_2 + q_3q_4) - a_y \\ 2(0.5 - q_2^2 - q_3^2) - a_z \end{bmatrix} \quad (18)$$

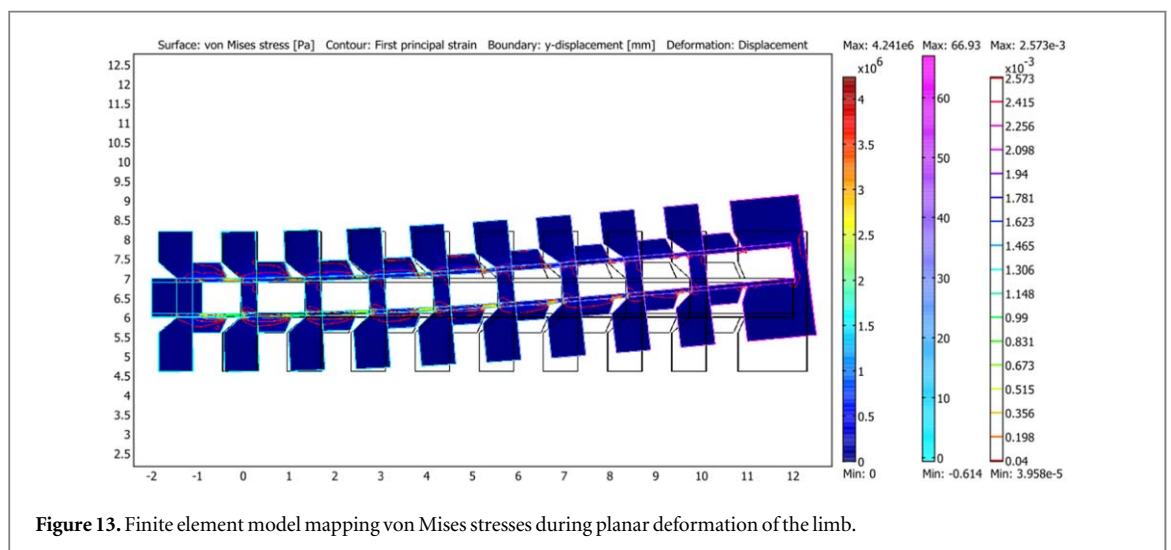
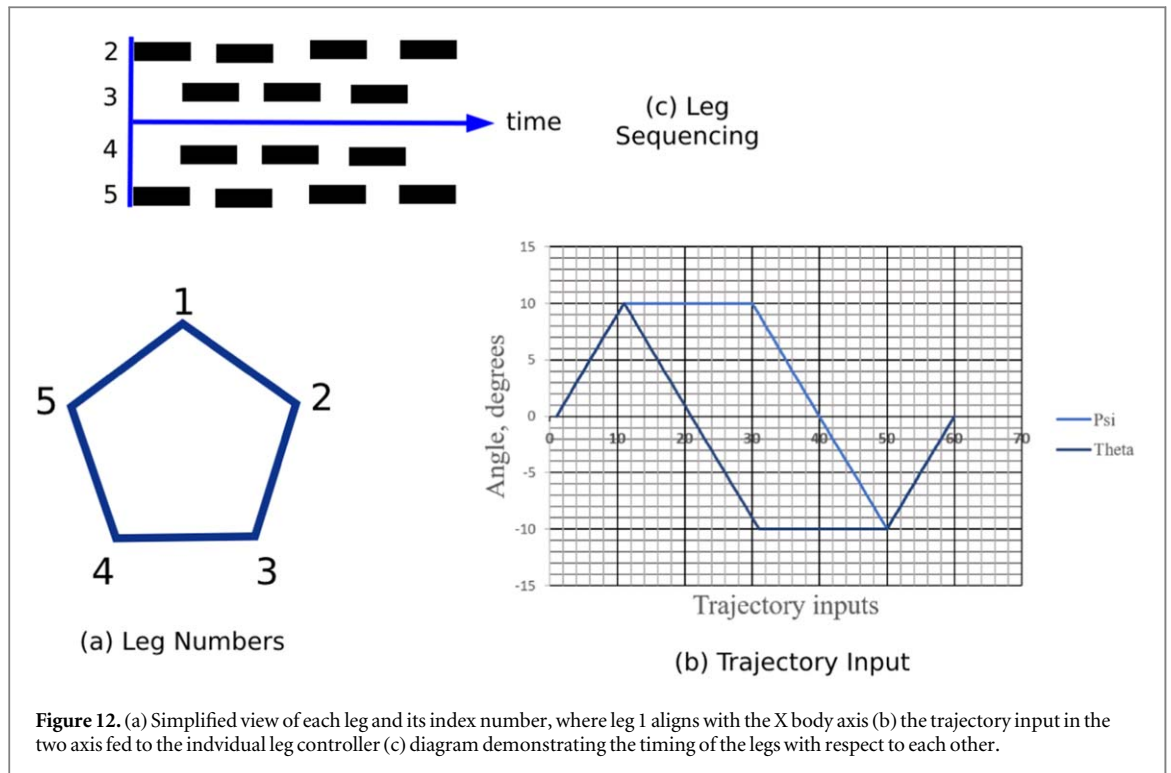
The Euler angle representation of the robots orientation can now be described by converting from quaternion representation to Euler angles. These are denoted by  $\Phi$ ,  $\Theta$ ,  $\Psi$ , which are the body orientations around the body axis  $Z$ ,  $Y$ ,  $X$  (in accordance with figure 11).

Gait scheduling was developed in accordance with that of the natural brittle star based on the work by [5] and [2], with minor modifications made to suit the kinematics of the system and to optimise gait performance. The observations of brittle star locomotion documented in [5], shows that the brittle star primary mode of locomotion is singular limb by singular limb. However, various video documentations [33, 34] also indicate that when swimming or traversing terrain at speed, a gait sequence similar to that shown in figure 12(c) is used, where the black rectangles represent the full cycle of motion as angles around the two limb axes, as shown in figure 12. This formed our initial proposed gait.

### 3. Results and discussion

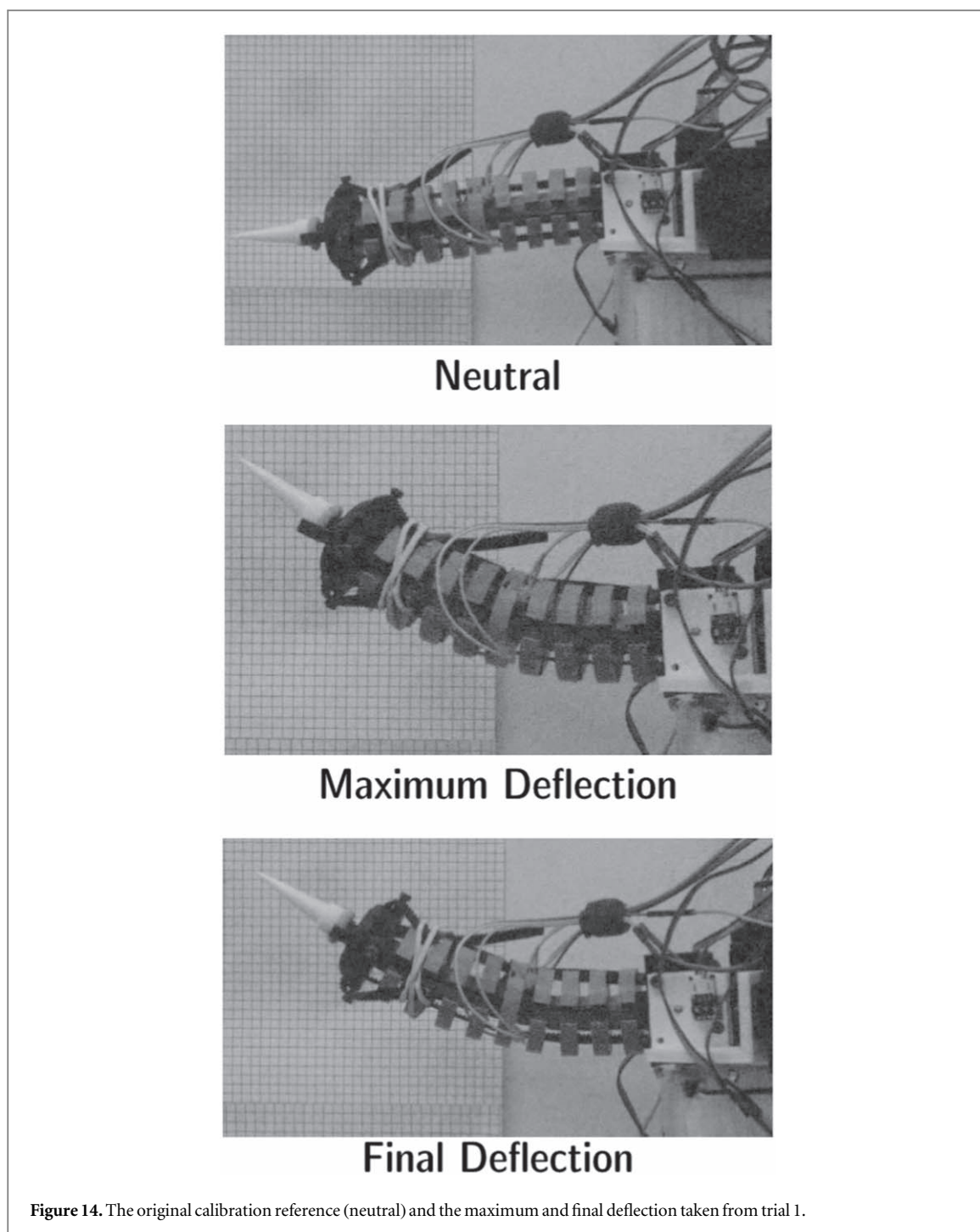
The limb deflected to a maximum of 66.93 mm from the numerical simulation results under a load of 21N, figure 13 and the resultant angle was 28.55°, which is within 2° of the expected 30° (i.e. 96% accuracy). In this figure, von Mises stresses are noted increase from tip to base, and reach a maximum of 4.24 MPa in the polypropylene, which is far below its yield strength of >12 MPa, evidencing that limb deformation remains elastically recoverable throughout its actuation cycle.

Quantifying the performance of the individual limb controller is vital to achieving more complex motion primitives and to the development of the body orientation controller. The controller designed and proposed by [30] was found to have an accuracy of 5.18° and 2.93° for the pitch ( $\theta$ ) and yaw ( $\phi$ ) error, respectively. Here, the limb was calibrated at a neutral position, figure 14. The vertical axis was provided a step input of 20°, and the horizontal axis given a reference signal of 0. The limb was filmed at 1000 Frames Per Second (FPS) with a 5mm reference grid background using a Chronos 1.4 (Krontech) high speed monochrome camera. The high speed



footage allowed us to find the exact frames where the maximum and final deflection angles occurred. These frames were then saved and the angle of the marker (white cone structure pictured in figure 14) recorded via the ImageJ software. Using this, an external measurement could be made to verify that the controller was performing as expected. This angle was measured in reference to the neutral position initially recorded, as that is what the feedback system deems as  $0^\circ$ . The micro-controller connected to the sensors recorded the sensor array derived angles,  $\theta$  and  $\psi$ . The PWM control signal for both motors was also recorded. This data was recorded at 50 kHz on the micro-controller. This process was repeated 8 times for a step response to  $+20^\circ$ , and the same again for  $-20^\circ$ .

From the plot (cf figure 15), the step response can be observed to be in line with what was expected. There was slight overshoot, but it reaches the steady state target within 10 000 cycles (0.2s). The limb was notably slower than expected at travelling between  $0^\circ$ – $2.5^\circ$ , a trend that was consistent with the other trials. This is likely due to assumptions made in the controller model that are different in real life. For example, the initial forces mean there is little vertical component, due to how the belt is fed through the arms it is pulling predominantly axially along the continuum until the angle of the belt begins to separate from the angle of the limb. This can even be observed in the final deflection of figure 14, where the gap between the belt and the limb appears larger than



the neutral belt position. The individual segments of the appendage's connected exoskeleton are able to freely rotate and as such the belts when tensioned as the motor torques ( $2.9 \text{ kg} \cdot \text{cm}$ ) enable realignment, and as such, the belts can reset themselves to the axis of the limb without disrupting the dynamics and accuracy of the appendage beyond an initial static movement. The PWM control signal at the initial portion of the curve is saturated, and because this response is a result of the system mechanics it is difficult to remedy. The overshoot could be fixed by varying the gains for less overshoot, but it is likely this would be at the cost of an aggressive response. Table 1, shows the difference between the desired angle and the final measured angle as observed from image analysis (Image J), along with the difference between the final measured angle and the measured angle. The former serving to validate the steady state error of the controller, and the latter to validate the sensor feedback method. The average steady state error of the step response is 1.895, a  $2.7 \times$  steady state error improvement to the control work proposed in [30]. This highlights two key benefits to the proposed continuum limb, the limb is able to be modelled and controlled without the need for a SVD compensator and the sensor feedback mechanism offers useful and accurate information for the controller. The design and experimentation

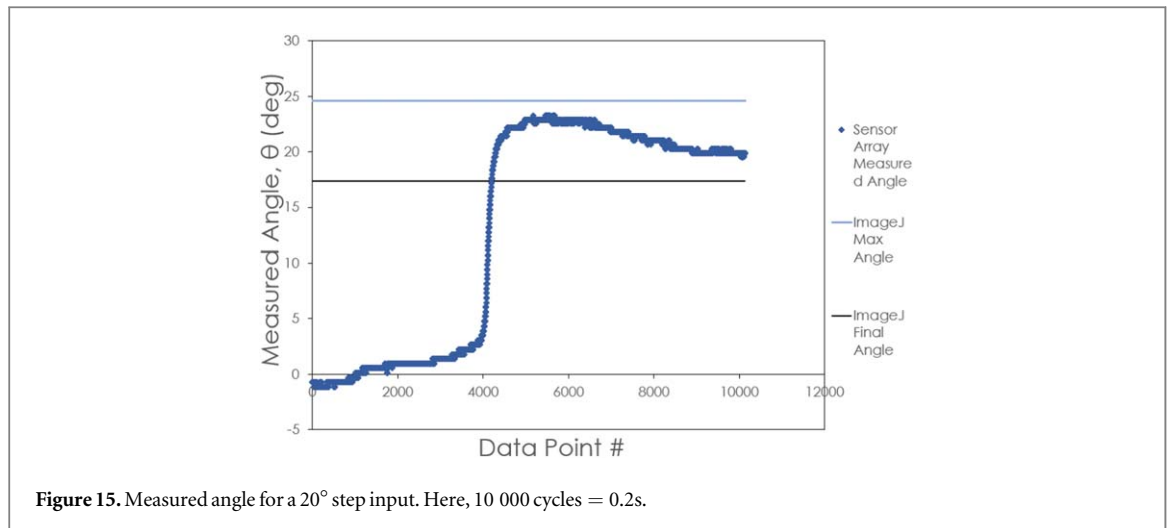


Figure 15. Measured angle for a 20° step input. Here, 10 000 cycles = 0.2s.

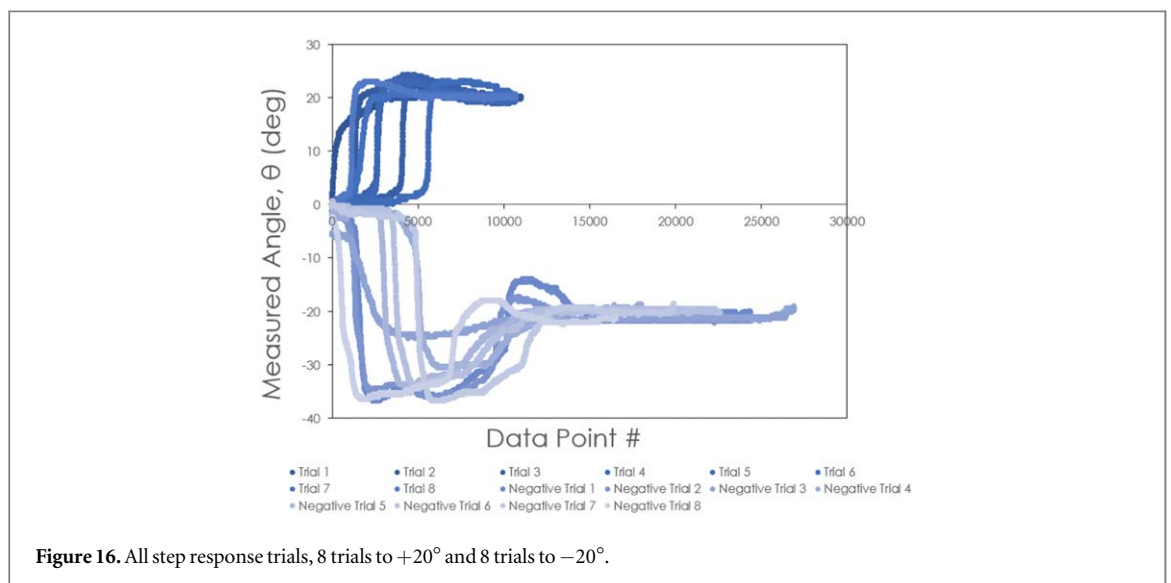


Figure 16. All step response trials, 8 trials to +20° and 8 trials to -20°.

Table 1. Error Data for the 8 trials with input +20°.

Trial #	ImageJ Angle to Step Input	ImageJ Angle to Sensor Angle
1	-0.52	0.38
2	-2.4	2.15
3	2.6	-2.52
4	1.8	-1.73
5	3.38	-2.6
6	3.3	-3.83
7	5.2	-5.65
8	1.8	-1.75
<b>Average</b>	1.89	-1.94
<b>Std. Deviation</b>	2.23	2.24

demonstrated here elucidates an alternative method for actuating soft-bodied robots that improves accuracy relative to the current reported methods for actuation.

From the collection of all trials, figure 16, all curves notably share similar shapes in both the positive and negative direction of motion. This indicates that the limb moves consistently upon step input requests. To validate this, we calculated the root mean squared error (RMSE) between the two most extreme curves (fastest initial response compared to slowest initial response). This is between the first and sixth trial in the positive direction. The RMSE was found to be 0.057. For the negative direction, trials 7 and 8 were compared and the

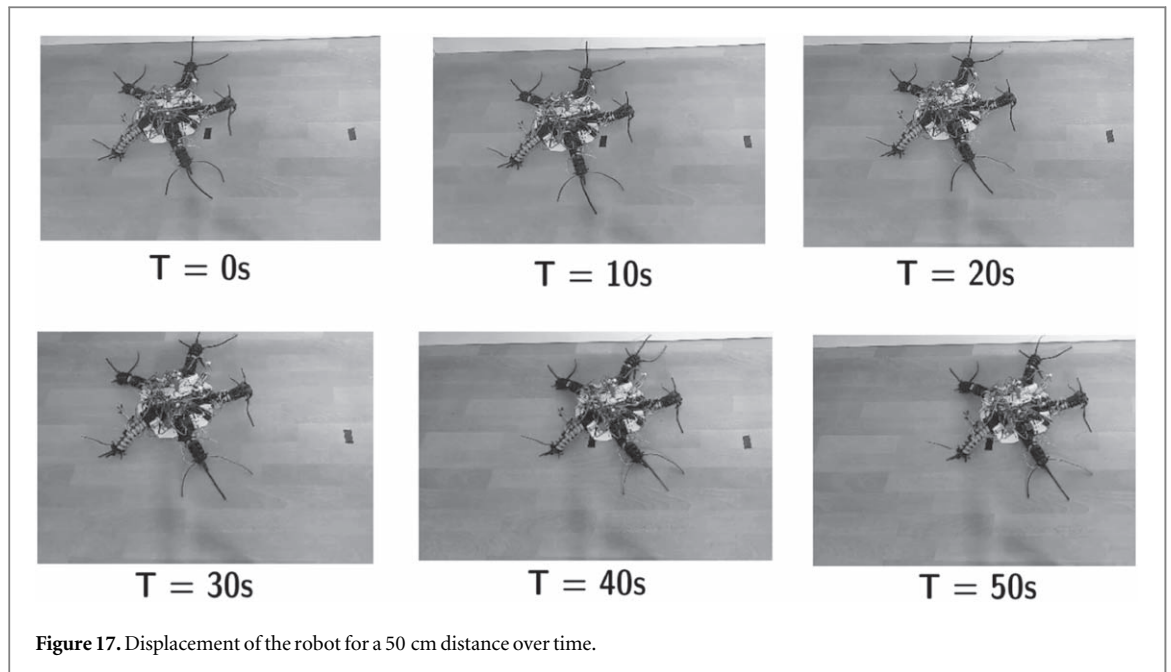


Figure 17. Displacement of the robot for a 50 cm distance over time.

Table 2. Comparison of displacements over time for brittle star inspired robots to the pentapod design from this work. Here:  $v$  is velocity,  $w$  is the weight of the robot and  $m$  is the momentum expressed by  $w \times v$ .

Robot	$v$ (m/s)	$w$ (kg)	$m$ (kg·m/s)	Power Source
Pentapod from this work	0.008	0.65	0.52	7.4v 450 mAh LiPo
PATRICK [4]	0.01	0.14	0.14	11.1v 300 mAh LiPo
Kano <i>et al</i> [5]	0.06	1.06	6.36	Tethered Power

resulting RMSE was 0.023. This indicates the curves are consistent with each other for a step response input of  $+20^\circ$  and  $-20^\circ$ . However, there is an observable difference between the shape of the positive and negative curves. The leg is essentially fighting gravity in the positive direction, whereas in the negative direction, the mass of the arm contributes to motion, behaviour that is not accounted for in the controller. Further work could be done to incorporate the mass of the arm segments as point masses along the arm that contribute to the inertial response of the arm under motion. In the context of the entire robot, the vertical axis of the limb will be responsible for lifting the robot, so it is anticipated that the curves would look different under a true loading scenario, but this experimentation serves to validate the Hall effect feedback mechanism and validates the consistency of the feedback loop to step response inputs. Figure 17 shows video frames taken at 10 second intervals from a video recorded using a Chronos 1.4 monochromatic video camera run at 1000fps. Table 2 provides some insight as to how the proposed design compares to existing both untethered (PATRICK [4]) and tethered ([5]) starfish inspired pentapod robots. In particular, we compare the velocity, weight and the momentum of each robot. The tethered robot from [5] unsurprisingly has the highest power and hence develops the highest momentum. PATRICK like the pentapod developed in this work, is an untethered pentapod. While PATRICK has a marginally higher velocity than our pentapod, it is also significantly lighter and as such, our robot exhibits a 3.7 times value for momentum than PATRICK.

#### 4. Conclusions

The results presented in this paper indicate the method of resolving orientation using a Hall effect sensor array configuration is effective. The data indicates the sensor is within  $2^\circ$  accurate at measuring the deflection angle of the leg for positions within a range of  $-20^\circ$  to  $20^\circ$ . This holds promise for the use of such a system in other continuum robotics. Current solutions for feedback control in continuum robotics measure the position of the drive motor, which relies on there being no slip between the drive and the continuum. This is, however, not the case when the continuum robot is under load since the sensors are integrated within the limb, they only take into consideration true limb motion, suggesting therefore, that the sensor array proposed herein, is a viable and effective method of resolving orientation in a continuum robot. When tested as a pentapod robot for velocity



and momentum, we find that the pentapod developed in this work has a lower velocity than another untethered pentapod (PATRICK) however, it is also significantly heavier and as such, its momentum is 3.7 fold higher than that of PATRICK.

## Data availability statement

The data that support the findings of this study are available upon reasonable request from the authors.

## ORCID iDs

Parvez Alam  <https://orcid.org/0000-0001-9122-9369>

## References

- [1] Stohr S, O'Hara T D and Thuy B 2012 Global diversity of brittle stars (echinodermata: Ophiuroidea) *PLoS One* **7** e31940
- [2] Tomholt L, Friesen L J, Berdichevsky D, Fernandes M C, Pierre C, Wood R J and Weaver J C 2020 The structural origins of brittle star arm kinematics: An integrated tomographic, additive manufacturing, and parametric modeling-based approach *J. Struct. Biol.* **211** 107481
- [3] Jin H, Dong E, Xu M, Liu C, Alici G and Jie Y 2016 Soft and smart modular structures actuated by shape memory alloy (sma) wires as tentacles of soft robots *Smart Mater. Struct.* **25** 085026
- [4] Patterson Z J, Sabelhaus A P, Chin K, Hellebrekers T and Majidi C 2020 An untethered brittle star-inspired soft robot for closed-loop underwater locomotion *2020 IEEE/RSJ International Conference on Intelligent Robots and Systems (IROS)*. IEEE pp 8758–64
- [5] Kano T, Sato E, Ono T, Aonuma H, Matsuzaka Y and Ishiguro A 2017 A brittle star-like robot capable of immediately adapting to unexpected physical damage *Royal Society Open Science* **4** 171200
- [6] Liu C, Sanfilippo F, Zhang H, Hildre H P, Liu C and Bi S 2012 Locomotion analysis of a modular pentapedal walking robot *Proceedings 26th European Conference on Modelling and Simulation (ECMS)* ed K G Troitzsch *et al* 441–7 ISBN: 978-0-9564944-4-3
- [7] Boscariol P, Henrey M A, Li Y and Menon C 2013 Optimal gait for bioinspired climbing robots using dry adhesion: a quasi-static investigation *J. Bionic Eng.* **10** 1–11
- [8] Autumn K *et al* 2005 Robotics in scansorial environments *Unmanned ground vehicle technology VII* 5804 (Bellingham, WA, USA: SPIE Digital Library) pp 291–302
- [9] Luo M, Skorina E H, Tao W, Chen F, Ozel S, Sun Y and Onal C D 2017 Toward modular soft robotics: proprioceptive curvature sensing and sliding-mode control of soft bidirectional bending modules *Soft Robotics* **4** 117–25
- [10] Tao W, Skorina E H, Chen F, McInnis J, Luo M and Onal C D 2015a Bioinspired design and fabrication principles of reliable fluidic soft actuation modules *2015 IEEE International Conference on Robotics and Biomimetics (ROBIO)* pp 2169–74
- [11] Yang H, Xu M, Li W and Zhang S 2019 Design and implementation of a soft robotic arm driven by sma coils *IEEE Trans. Ind. Electron.* **66** 6108–16
- [12] Abah C, Orekhov A L, Johnston G L H and Simaan N 2022 A multi-modal sensor array for human-robot interaction and confined spaces exploration using continuum robots *IEEE Sensors J.* **22** 3585–94
- [13] Ur Rehman A, Mack J and Alam P 2022 From e-waste to robots: a case study on e-waste upcycling in low-to-middle income countries *2021 IEEE International Humanitarian Technology Conference (IHTC)*. IEEE Xplore pp 1–4
- [14] Alam P 2020 Hacking into e-waste *Mater. World* **28** 24–7
- [15] McMahan W, Jones B A and Walker I D 2005 Design and implementation of a multi-section continuum robot: Air-octor *2005 IEEE/RSJ International Conference on Intelligent Robots and Systems*. IEEE pp 2578–85
- [16] Walker I D 2013 Continuous backbone 'continuum' robot manipulators *International Scholarly Research Notices* **2013** 726506
- [17] Nguyen T-D and Burgner-Kahrs J 2015 A tendon-driven continuum robot with extensible sections *2015 IEEE/RSJ International Conference on Intelligent Robots and Systems (IROS)*. IEEE pp 2130–5
- [18] Gravagne I A, Rahn C D and Walker I D 2003 Large deflection dynamics and control for planar continuum robots *IEEE/ASME Trans. Mechatron.* **8** 299–307
- [19] Webster R J III and Jones B A 2010 Design and kinematic modeling of constant curvature continuum robots: A review *The International Journal of Robotics Research* **29** 1661–83
- [20] Hannan M W and Walker I D 2003 Kinematics and the implementation of an elephant's trunk manipulator and other continuum style robots *J. Robot. Syst.* **20** 45–63
- [21] Godage I S, Nanayakkara T and Caldwell D G 2012 Locomotion with continuum limbs *2012 IEEE/RSJ International Conference on Intelligent Robots and Systems*. IEEE pp 293–8
- [22] Sun Y, Jiang Y, Yang H, Walter L-C, Santoso J, Skorina E H and Onal C 2020 Salamanderbot: a soft-rigid composite continuum mobile robot to traverse complex environments *2020 IEEE International Conference on Robotics and Automation (ICRA)*. IEEE pp 2953–9
- [23] Yang H, Xu M, Li W and Zhang S 2018 Design and implementation of a soft robotic arm driven by sma coils *IEEE Trans. Ind. Electron.* **66** 6108–16
- [24] Trivedi D, Rahn C D, Kier W M and Walker I D 2008 Soft robotics: biological inspiration, state of the art, and future research *Appl. Bionics Biomech.* **5** 99–117
- [25] Ozel S, Keskin N A, Khea D and Onal C D 2015 A precise embedded curvature sensor module for soft-bodied robots *Sens. Actuators, A* **236** 349–56
- [26] Tao W, Skorina E H, Chen F, McInnis J, Luo M and Onal C D 2015b Bioinspired design and fabrication principles of reliable fluidic soft actuation modules *2015 IEEE International Conference on Robotics and Biomimetics (ROBIO)*. IEEE pp 2169–74
- [27] Cichon D and Psiuk R 2016 Model-based characterization of permanent magnets with a 3d hall-sensor array *2016 VI International Electric Drives Production Conference (EDPC)*. IEEE pp 238–43
- [28] Yan L *et al* 2014 An orientation measurement method based on hall-effect sensors for permanent magnet spherical actuators with 3d magnet array *Sci. Rep.* **4** 1–8
- [29] Girgin A, Bilmez M, Amin H Y and Karalar T C 2019 A silicon hall sensor soc for current sensors *Microelectron. J.* **90** 12–8

- [30] Patterson Z J, Sabelhaus A P and Majidi C 2022 Robust control of a multi-axis shape memory alloy-driven soft manipulator *IEEE Robotics and Automation Letters* **7** 2210–7
- [31] DesignerData. Polyprylene, 2010. Available at: [https://designerdata.nl/materials/plastics/thermo-plastics/polypropylene-\(cop.\)](https://designerdata.nl/materials/plastics/thermo-plastics/polypropylene-(cop.)).
- [32] Madgwick S *et al* 2010 An efficient orientation filter for inertial and inertial/magnetic sensor arrays *Report x-io and University of Bristol (UK)* **25** 113–8
- [33] 2011ACVVV. Noaa may 05—brittle star catches a squid!, 2017. Available at: <https://www.youtube.com/watch?v=B1F81BkFl2U>.
- [34] NOAA Office of Ocean Exploration and Research. Rare video of brittle star swimming in deep ocean, 2018. Available at: <https://www.youtube.com/watch?v=ejk-R-LPFys>.